



Particles II

Access the latest eBook →

11

Advanced
Optical Metrology

Particles II



EVIDENT
OLYMPUS

WILEY

Impact on Biological Systems and the Environment

This eBook is dedicated to the research of Professor David Wertheim.

In collaboration with various groups, Professor Wertheim uses confocal microscopy to analyse the impact of different types of particles on human health and the environment, with a focus on human health-hazardous particles detected with solid-state nuclear track detectors (SSNTD). Download for free, today.

EVIDENT
OLYMPUS

WILEY

An Iontronic Multiplexer Based on Spatiotemporal Dynamics of Multiterminal Organic Electrochemical Transistors

Dimitrios A. Koutsouras,* Morteza Hassanpour Amiri, Paul W. M. Blom, Fabrizio Torricelli,* Kamal Asadi, and Paschalis Gkoupidenis*

The seamless integration of electronics with biology requires new bio-inspired approaches that, analogously to nature, rely on the presence of electrolytes for signal multiplexing. On the contrary, conventional multiplexing schemes mostly rely on electronic carriers and require peripheral circuitry for their implementation, which imposes severe limitations toward their adoption in bio-applications. Here, a bio-inspired iontronic multiplexer based on spatiotemporal dynamics of organic electrochemical transistors (OECTs), with an electrolyte as the shared medium of communication, is shown. The iontronic system discriminates locally random-access events with no need of peripheral circuitry or address assignment, thus decreasing significantly the integration complexity. The form factors of OECTs that allow for intimate biointerfacing as well as the electrochemical nature of the communication medium, open new avenues for unconventional multiplexing in the emerging fields of bioelectronics, wearables, and neuromorphic computing or sensing.

stems from the ability of electronics to bi-directionally interact with biological systems, and even more importantly to emulate biological functions, thus, allowing seamless communication and integration.^[3,4] Biological systems—including animals and plants—communicate and process information using as carriers ions, small molecules, and electronic charges.^[5] In the nervous system, stimuli are collected from distributed sensory receptors, computation then takes place locally or centrally, and when necessary, feedback signals drive sensorimotor processes.^[5] Interestingly, within this loop, biological systems perform sensing, computing, and actuation by means of temporal and spatial multiplexing of information. For instance, nerve fibers in the peripheral nervous system carry and

multiply bio-signals from sensory neurons.^[6] Even single neurons are able to discriminate via multiplexing, spatiotemporal sequences of incoming signals that are distributed across their dendrites.^[7,8] At a higher level, brain oscillations are known to coordinate or even multiplex the flow of temporally asynchronous biological events,^[9–11] but are not strictly considered to be global clocks as they are spatially distributed across the brain and diversify in the frequency domain.^[9,12] Such spatiotemporal multiplexing paradigms in biological systems are not only inherently dependent on the structure of biological neural networks, but also on the surrounding medium, namely a global aqueous environment that in the simplest case is salt water.^[5,13]

Although conventional multiplexing schemes are successful in numerous applications, it is apparent that seamless integration between electronic and biological systems requires new bio-inspired approaches that, analogously to nature, inherently rely on ionic–electronic (i.e., iontronic) materials and devices, or even system architectures. Inspired from biology and motivated by the need of simplicity and minimalism in multiplexing concepts, iontronic systems that exhibit spatiotemporal response have the potential for compact multiplexing of time-domain signals, as spatial specificity of signal sources is inherently embedded into their device dynamics. Toward this direction, organic electrochemical transistors (OECTs) are promising candidates for bio-inspired electronics because they show stable operation in electrolytes (both liquid or soft solid-state electrolytes), and owing to their volumetric ionic–electronic charge

1. Introduction


The integration of electronics with biology is triggering significant attention in several fields, including medical diagnostics, personalized and precise medicine, healthcare, bioelectronics, and biorobotics.^[1,2] The technological potential of such co-integration

Dr. D. A. Koutsouras, M. H. Amiri, Prof. P. W. M. Blom, Prof. K. Asadi, Dr. P. Gkoupidenis

Max Planck Institute for Polymer Research
Ackermannweg 10, Mainz 55128, Germany
E-mail: koutsouras@mpip-mainz.mpg.de;
gkoupidenis@mpip-mainz.mpg.de

Prof. F. Torricelli
Department of Information Engineering
University of Brescia
Brescia 25123, Italy
E-mail: fabrizio.torricelli@unibs.it

Prof. K. Asadi
Department of Physics
University of Bath
North Road, Claverton Down, Bath BA2 7AY, UK

 The ORCID identification number(s) for the author(s) of this article can be found under <https://doi.org/10.1002/adfm.202011013>.

© 2021 The Authors. Advanced Functional Materials published by Wiley-VCH GmbH. This is an open access article under the terms of the Creative Commons Attribution License, which permits use, distribution and reproduction in any medium, provided the original work is properly cited.

DOI: 10.1002/adfm.202011013

interaction taking place in the whole bulk of the polymer, OECTs offer an ideal platform for compact multiterminal configurations^[38–43] as well as facile and highly efficient biointerfacing.^[43] In addition, the ion transduction of OECTs combined with their neuromorphic properties,^[21,41] render them as an ideal technology platform for numerous applications including bioelectronics, neuro-inspired processing, and sensing.^[21,41,44–46]

On the contrary, in traditional electronic systems, electron conductive paths (e.g., metal lines) are used to connect the various parts of the system. Applications with restrictions in space, cost, and energy resources require the compact signal transmission between circuit components. For instance, when a multitude of elements is necessary (i.e., sensors, actuators, and memory), the most affordable structure is the cross-bar matrix integration. In this approach, an arbitrary number of $M \times N$ elements are organized in a device grid of M rows and N columns, which require $M + N$ metal lines for the interconnections. Prominent examples of matrix-like electronic multiplexing include displays (e.g., row/column addressing of lighting pixels),^[14–16] cross-bar arrays of analogue memories in neuromorphic computing (e.g., dot product or weighted multiplexing of rows across a column),^[17–22] electrode arrays for electrophysiological recording/stimulation, and physical (e.g., pressure, temperature, and light), chemical, and biological sensor arrays.^[23–26]

Many of these multiplexing approaches rely on extensive accessing/read-out peripheral circuitry and accurate timing/synchronization protocols that require significant computational resources. Another possible approach, when applicable, is based on the passive addressing where a matrix is solely made of devices with rectifying properties.^[22] Although of compact structure, this addressing scheme requires a concurrent combination of biasing conditions and therefore central clocks and controllers for coordination.^[22,27,28] In order to simplify the addressing conditions, methods based on frequency-division multiplexing in passive matrices have been successfully implemented in electronic bio-signal acquisition.^[29] However, signal reconstruction requires complex peripheral circuitry for phase detection. Active addressing necessitates access elements in close proximity to the various devices of the matrix, thus significantly increasing the integration complexity. Indeed, such cross-bar arrays minimize undesirable cross-talk/parasitic communication, but still require nonlinear access elements such as transistors or diodes for addressing a device or a whole row/column.^[22] Multiplexing with active addressing, in many cases still needs to be coordinated by central clocks.^[14] Pseudo-parallel access with high scan-rates of sequential row-by-row addressing (time-division multiplexing) relaxes partially the need for time coordination in biosensing and lighting display applications, but still high-speed peripheral electronics are necessary.^[15,16,23] This pseudo-parallel method requires over-scanning with high-speed rates and, as a consequence, it is power-hungry (with idle power consumption), especially if employed for temporally and spatially sparse or even asynchronous input sources and signals found in biological neural activities and sensory systems.^[30–33]

An alternative approach is the event-based signaling—loosely considered as a form of code-division multiplexing—where inputs are encoded and transmitted through a shared medium only when it is necessary, meaning asynchronous or clock-

less transmission.^[34–37] Therefore, event-based signaling is an energy efficient multiplexing scheme when dealing with sparsity, and has been successfully incorporated in e-skins based on soft electronics for the emulation of tactile sensing.^[25] This approach allows for asynchronous communication between sensing and processing modalities by multiplexing input signals via a common conductor.^[25] Nevertheless, it is still a multiplexing scheme of address encoding with signal reconstruction that requires off-chip decoding, and the use of the common conductor as a signal collector also implies the absence of spatial specificity of a signal source. On the contrary, spatial specificity is inherently embedded in the dynamics of iontronic devices and systems.

Here, we show a bio-inspired iontronic multiplexer based on spatiotemporal dynamics of multiterminal OECTs. Analogously to biological systems, an electrolyte serves as the shared medium of communication and owing to the spatial dependence of the ionic–electronic coupling, the proposed system is able to discriminate locally random-access events at the input terminals with no need of address encoding or specialized peripheral circuitry. In this way, we demonstrate the multiplexing of 25 signals by means of a simple polymeric channel. The system is modeled by using a physically based circuit-aware approach and the model is implemented in an industrial-standard circuit simulator. The simulations are able to predict the system behavior, providing insight on the key system parameters for spatiotemporal dynamics and the model represents a universal platform for a greater family of materials. The proposed approach opens new avenues for minimalistic, ion-based multiplexing, when circuitry simplicity for signal transfer is essential, including applications in the emerging fields of bioelectronics, wearable electronics, neuromorphic computing, and sensing.

2. Results and Discussion

A schematic of the iontronic multiplexer is shown in **Figure 1a**. The system consists of a channel made of the conducting polymer blend poly(3,4-ethylenedioxythiophene) doped with poly(styrene sulfonate) (PEDOT:PSS). PEDOT:PSS is a high-performance p-type conductive polymer, consisting of a hole conductive PEDOT blended with the ion conductive PSS.^[43,47] Therefore, PEDOT:PSS supports both electronic and ionic transport and is termed as organic mixed ionic–electronic conductor.^[47] When a PEDOT:PSS film is in contact with an electrolyte, ions can permeate the polyelectrolyte phase and ionic–electronic charge compensation takes place through the whole bulk volume of the polymer.^[48] As a result, the electronic (hole) charge density into the PEDOT semiconducting phase of the polymer is electrochemically modulated by injecting ionic carriers from/to the electrolyte into the PSS phase of the polymer, depending on the voltage of the gate electrode. This ionic-to-electronic current modulation constitutes the principle of operation of OECTs.^[43,49] Here, the PEDOT:PSS channel is electrostatically coupled via an electrolyte (NaCl at various concentrations) with a grid of 5×5 electrodes which acts as gates. Therefore, the iontronic multiplexer consists of a multiterminal OECT. The gate electrodes are made of gold (Au) covered with PEDOT:PSS providing electronic-to-ionic signal conversion. The

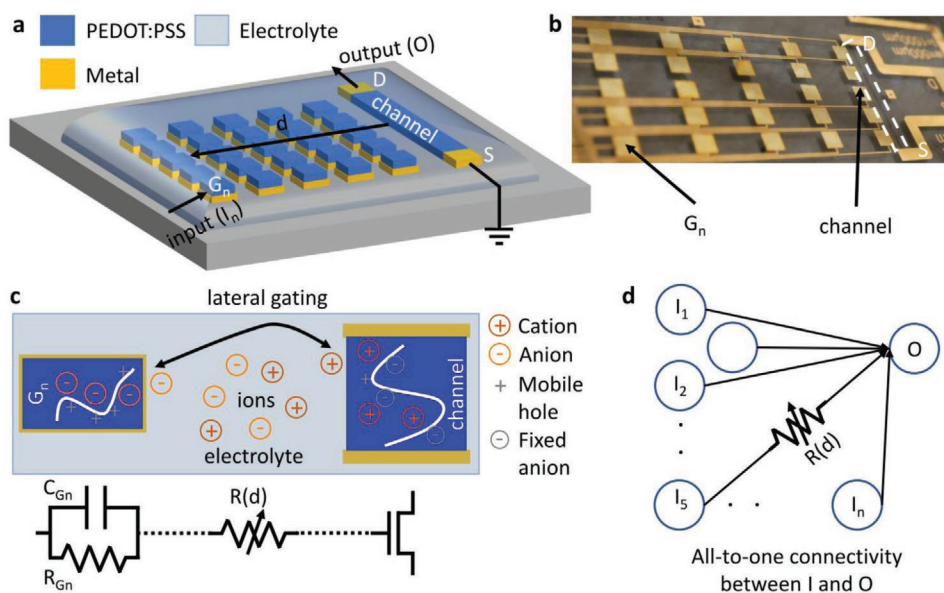


Figure 1. Iontronic multiplexer based on spatiotemporal dynamics of multiterminal OECTs. a) Schematic of the device structure of the iontronic multiplexer. The multiplexer is a multiterminal organic electrochemical transistor (OECT), consisting of a polymer channel (between source: S and drain: D electrodes) based on the conducting polymer PEDOT:PSS. The channel is gated via an electrolyte with a regular grid of 5×5 metal gates, G_n ($n = 1-25$), covered with PEDOT:PSS. The electrolyte serves as a connectivity medium between the gates, G_n , and the channel. The grid of gates, G_n , serves an array of inputs I_n , while the output O of the channel is accessed by the drain electrode D . The G_n gates are spatially distributed across the device structure. b) Optical image of a fabricated multiterminal OECT. c) Top-view schematic of the ionic–electronic coupling of a G_n –channel pair and the corresponding equivalent circuit. The OECT channel is coupled with a gate of capacitance C_{G_n} and resistance R_{G_n} via the electrolyte with resistance $R(d)$. Owing to the spatial configuration between the gates and channel, the electrolyte resistance exhibits spatial properties and depends on the gate–channel distance $R(d)$. d) The device configuration, in combination with the connectivity medium, results in an all-to-one connectivity between device inputs (I_n) and the output O .

device microfabrication process is described with more details in the Experimental Section. In this system configuration, input voltage signals (I_n) are applied at a gate electrode, G_n , while the output current (O) is measured at the drain electrode of the multigate OECT. It is worth noting that in a real biointerfacing or biological system the gate could be replaced by a distributed sensor or a local bio-signal generator entity. The shared electrolyte between the gates, G_n , and the channel allows for “parallel” coupling of the channel with the various gates, G_n .^[39,40,50] An actual microfabricated device is displayed in Figure 1b.

A subsection of the multiterminal OECT comprising a gate, G_n , and the channel is depicted at Figure 1c. When an input voltage signal is applied at the gate electrode, ions drift from the bulk of the electrolyte toward G_n and the channel. More in detail, a positive bias at the gate leads to the drift of cations via lateral gating into the channel. Cations compensate the sulfonic acid groups of PSS^- (fixed anions) close to the $PSS/PEDOT$ interface and this, in turn, leads to a decrease of the hole density into the PEDOT. The opposite situation is observed at the G_n gate electrode that is also covered with PEDOT:PSS. The ions flowing into the electrolyte can be described by an ionic resistor where the resistivity per unit area depends on the ion mobility, which is an intrinsic property of the electrolyte, while the area and length (d) of the resistor can be selected by design. As a result, the electrostatic ionic–electronic coupling of the gate–electrolyte–channel can be described by the simplified circuit diagram showed in Figure 1c. The volumetric electric-double-layer capacitance at the gate is described with a capacitor C_{G_n}

and the resistor R_{G_n} connected in parallel expresses any electronic or ionic loss mechanism (in $Au/PEDOT:PSS$ electrodes R_{G_n} is usually high,^[48] and could be omitted^[51,52]). The drift of ions into the electrolyte is described by a distance-dependent resistor $R(d)$, and the ionic–electronic coupling between the electrolyte and the channel is described with a volumetric transistor. Owing to the spatial distribution of the gates in respect to the channel, the electrolyte resistance depends on the input–output distance, d , between G_n and the channel. Hence, $R(d)$ in the multiterminal OECT system configuration is a variable (distance dependent) resistor. Owing to the common nature of the electrolyte, this ionic–electronic coupling holds in parallel for every G_n –channel pair of the multiterminal OECT. The common electrolyte results in an all-to-one connectivity topology between the inputs I_n and the output O , with a spatially dependent coupling modality. The ionic–electronic coupling of the multiterminal OECT is translated into a connectivity diagram as shown in Figure 1d (for simplicity purposes, the gate-to-gate cross-coupling is omitted from the diagram). This connectivity diagram is used for the implementation of the iontronic multiplexer using spatiotemporal device dynamics.

The device geometric configuration leading to spatiotemporal response is investigated in Figure 2. The electrochemical parameters of the system are measured by probing the impedance spectrum (IS) of the multiterminal OECT device with channel of variable-sized active area. In Figure 2a,b, a large channel device with an area (Width \times Length), $W \times L = 500 \times 15\,000 \mu m^2$, is investigated, and in Figure 2c,d, a small channel device with an

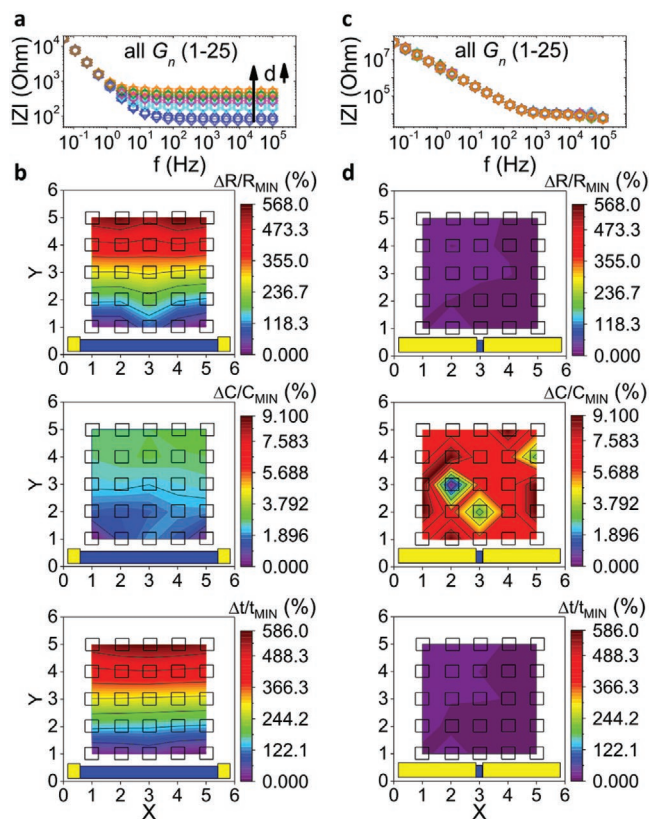


Figure 2. System configuration for spatiotemporal response. Large channel: a) Amplitude of impedance spectrum ($|Z|$ vs f) of all G_n -channel pairs ($n = 1-25$). b) Spatial mapping of the ionic resistance R , interfacial capacitance C , and the corresponding response time $\tau = R \cdot C$ for all G_n -channel pairs after modeling the IS with an equivalent circuit consisting of a resistor and a capacitor in series (RC). R , C , and τ are represented as relative variation ($\Delta R/R_{\text{MIN}}$, $\Delta C/C_{\text{MIN}}$, $\Delta \tau/\tau_{\text{MIN}}$). Small channel: c) $|Z|$ versus f of all G_n -channel pairs. d) Spatial mapping of R , C , and τ (relative variation) for all G_n -channel pairs. The spatiotemporal response is evident for the case of the large channel, while in the case of the small channel the spatiotemporal phenomena are heavily suppressed. An aqueous NaCl electrolyte with concentration, $c = 100$ mM, is used for the measurements. Large channel device: channel dimensions ($W \times L = 500 \times 15\,000 \mu\text{m}^2$), gate dimensions: ($A_G = 2000 \times 2000 \mu\text{m}^2$). Small channel device: channel dimensions ($W \times L = 20 \times 20 \mu\text{m}^2$), gate dimensions ($A_G = 2000 \times 2000 \mu\text{m}^2$).

area, $W \times L = 20 \times 20 \mu\text{m}^2$, is investigated as reference. The 5×5 gate grid has the very same dimensions in both cases and the detailed system geometries are shown in the Figure S1, Supporting Information. The IS is probed between each gate, G_n , and the channel. The corresponding equivalent circuit is shown in the Supporting Information. For each G_n -channel pair, the ionic resistance R and ionic-electronic volumetric capacitance C are extracted using equivalent circuit modeling.^[48,51] The spatial mappings of R , C , and of the characteristic response time $\tau = R \cdot C$ are then obtained.

In the case of large channel devices, Figure 2a shows that the IS measured by varying the gate-channel distance are different when the frequency of the input signal is larger than few Hz. The corresponding spatial mappings of the ionic resistance R , volumetric capacitance C , and time constant τ (presented as relative variation) displayed in Figure 2b clearly

demonstrate that the IS is dominated by the electrolyte resistance R , which increases by increasing the gate-channel distance (Figure S2, Supporting Information). We found that in large channel devices the maximum relative variation amounts to $\Delta R/R_{\text{MIN}} = 560\%$. In contrast, in the case of small channel devices, Figure 2c shows that the IS spectra are almost perfectly overlapping for all G_n -channel pairs ($n = 1-25$), and the corresponding spatial mappings of R , C , and τ are only weakly dependent on the spatial device configuration. In more detail, Figure 2d shows that the maximum relative variation of is: $\Delta R/R_{\text{MIN}} < 20\%$, $\Delta C/C_{\text{MIN}} < 10\%$, and $\Delta \tau/\tau_{\text{MIN}} < 20\%$, respectively. The measured values are displayed in Figure S2, Supporting Information. In both cases of small and large channels, C is practically independent of the G_n positions ($\Delta C/C_{\text{MIN}} < 10\%$). This is attributed to the fact that interfacial capacitance C corresponds to the low frequency regime of the spectrum, therefore it is defined by the interfaces (practically the same interfaces for different G_n -channel couples) and not by the electrolyte. The response time, τ , follows the trend of R . Comparing the measured R and C displayed in Figure S2b,d, Supporting Information, we found that the ionic resistance R of the small channel system is about one order of magnitude larger than R measured in the large channel system. This explains the limited relative variation, $\Delta R/R_{\text{MIN}}$, in the case of the small channel system, and indicates that the ionic resistance significantly depends on the geometrical properties of the channel. This experimental analysis clearly shows that the dimension of the polymeric channel is a key system parameter, since it significantly impacts on both the gate-channel ionic resistance and the channel capacitance itself. Importantly, the proper sizing of the channel enables the enhancement of the spatiotemporal response of the system while the electrolyte connectivity medium tunes the spatiotemporal response.

The scaling behavior of the ionic resistance R as a function of the G_n -to-channel distance d (central column of the 5×5 gate grid) is presented at Figure 3a, in the case of the large channel and small channel as reference. The spatial scaling of the ionic resistor is evident for the large channel, while the effect is negligible for the small channel configuration. Figure 3b focuses on the large channel, displaying the spatial scaling of R for various electrolyte concentrations ($c = 5-500$ mM NaCl). As expected, R scales linearly with d for all ionic concentrations, $R \approx d$. Despite the fact that the two interfaces, G_n /electrolyte and electrolyte/channel are lateral (integrated on the very same substrate), with different areas, and with a “virtual” cross section of the ionic conductor (i.e., the electrolyte) to be loosely defined, linear scaling indicates an exemplar Ohm’s law behavior. The configuration of the multiterminal OECT device with the 5×5 G_n grid, suggests the formation of 25 “virtual” and parallel wires between the G_n -channel terminals via the electrolyte medium. In addition, it is worth noting that also all the various gates are connected (25 \times 25 connections) through the electrolyte. For evaluating the linear scaling behavior in Figure 3b, a modified formulation of a conductor with variable cross-sectional area,

A_1 to A_2 , is used ($R = \rho \frac{d}{\sqrt{A_1 A_2}} + R_0$, refer to the Supporting Information), with R_0 the residual resistance obtained when $d = 0$.^[53] The resistivity ρ of the “virtual” wire is calculated for $c = 100$ mM NaCl and amounts to $\rho = 8.1$ Ohm \cdot cm. It should

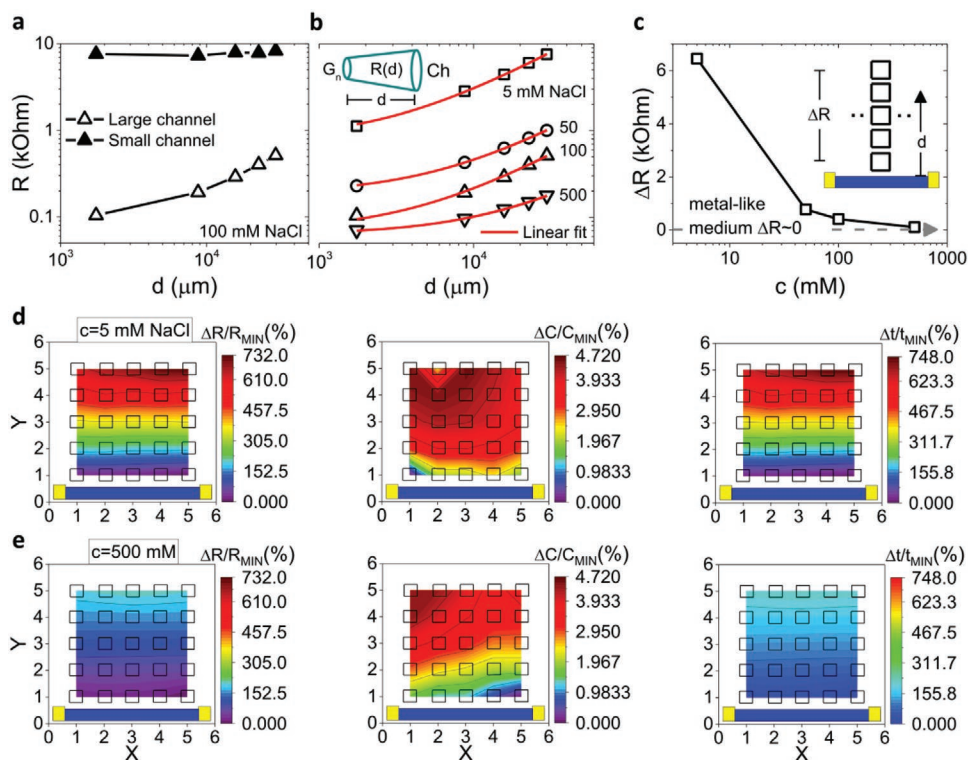


Figure 3. Spatial scaling of the connectivity medium. a) Ionic resistance R ($X = 3$, $Y = 1-5$) as a function of the gate-to-channel distance, d , for the large and small channel ($c = 100$ mM NaCl). The dependence of R on d is much stronger in the case of the large channel. b) Ionic resistance, R , as a function of d for $c = 5-500$ mM NaCl, in the case of the large channel. R scales linearly with d for all concentrations suggesting a simple Ohm's law behavior (here shown in logarithmic scale for clarity). c) Maximum resistance difference ΔR of the central gate column between the most distant and the closest gate electrode as a function of c . Spatiotemporal response and connectivity medium. Spatial mapping of the relative variation of R , C , and τ for all G_n -channel pairs and for $c = 5-500$ mM NaCl. d) $c = 5$ mM NaCl. e) $c = 500$ mM NaCl. Large channel device: channel dimensions ($W \times L = 500 \times 15\,000 \mu\text{m}^2$), gate dimensions: ($A_G = 2000 \times 2000 \mu\text{m}^2$). Small channel device: channel dimensions ($W \times L = 20 \times 20 \mu\text{m}^2$), gate dimensions ($A_G = 2000 \times 2000 \mu\text{m}^2$).

be noted that the calculated value is an effective resistivity for the designed system and it cannot be directly related to the intrinsic electrolyte resistivity (≈ 100 Ohm·cm for $c = 100$ mM NaCl), as the system consists of in-plane interfaces; a situation that differs from an ideal parallel plate capacitor. Moreover, the analysis provides the residual resistance which amounts to $R_0 = 68$ Ohm.

The electrolyte serves as connectivity medium and it can tune the spatiotemporal response of the multiterminal system when the system is suitably designed. The maximum variation of the electrolyte resistance ΔR across the Y -direction as a function of the electrolyte concentration, c , is shown in Figure 3c. The measurements show that for highly conductive connectivity media that approach metal conductivity, the spatiotemporal response of the system is heavily suppressed. More specifically, Figure 3d,e shows the spatial mappings of relative variation of R , C , and τ resulting from the equivalent circuit analysis of the IS spectrum for all G_n -channel pairs, for two cases of electrolyte concentration (low: $c = 5$ mM, high: $c = 500$ mM NaCl). As expected, in both cases the relative variation of the volumetric capacitance ($\Delta C/C_{\text{MIN}}$) across the device footprint is minor, as it primarily depends on the low frequency IS response of a G_n /channel pair. In contrast, the relative variation of the ionic resistance $\Delta R/R_{\text{MIN}}$ (and therefore of the corre-

sponding τ) is more pronounced for lower ionic concentrations of the electrolyte. This can be explained as follows. At low ion concentration, the ionic resistance dominates in a wide range of the IS compared to the volumetric capacitance, and the spatiotemporal dynamics of the multiterminal system are emerging. Figure 3d,e demonstrates clearly that spatiotemporal phenomena are more pronounced for less-conductive connectivity media and in contrast with current approaches,^[25] spatial specificity of (sensory) signal sources can be introduced locally by collecting signals via media of relatively low ionic conductivity.

By closely observing representative IS spectra of the multiterminal OECT for the G_n -channel pairs, specific frequency-dependent modes of operation can be identified (Figure 4). Conventional current-voltage (I - V) curves with slow sweep rates (< 200 mV s^{-1} , $f_{\text{eff}} < 0.3$ Hz), such as output characteristics of the multiterminal device (drain current vs gate voltage, I_D vs V_G), are effective low-frequency measurements. On the contrary, pulsing the G_n gate(s) effectively probes the high-frequency device dynamics (for a pulse width ≤ 100 ms, $f_{\text{eff}} \geq 10$ Hz) in the I_D versus time response. Under such temporal conditioning, the response of the multiterminal OECT displays readily observable spatiotemporal response. In the case of the large channel (Figure 4a), the IS spectra for three representative G_n -channel pairs (small, medium, and far

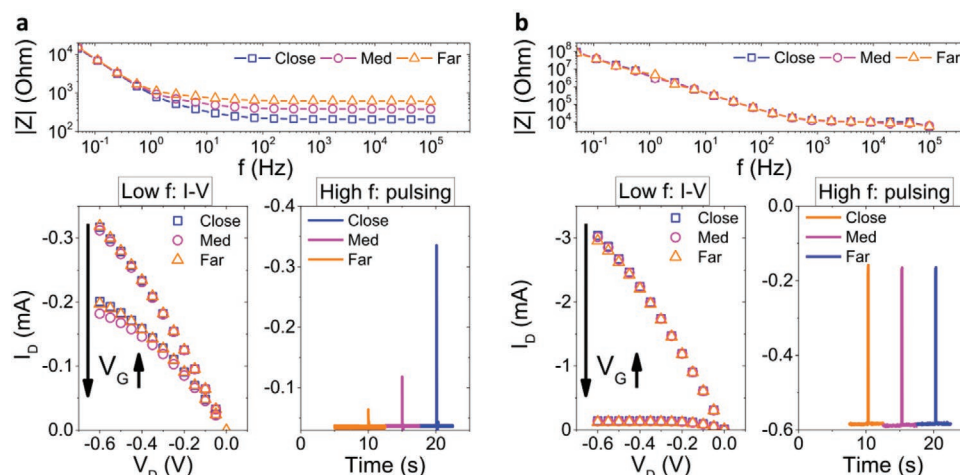


Figure 4. Frequency-dependent modes of operation. a) Large channel. $|Z|$ versus f spectrum for three gate–channel pairs: close distance ($X = 3$, $Y = 1$), medium distance ($X = 3$, $Y = 3$), and far away distance ($X = 3$, $Y = 5$). $|Z|$ versus f merges into a single curve for low frequencies f , while it is increasing with the G_n -channel distance at higher f . Low f (quasi-static) output characteristics I_D versus V_D , and high f pulsing response (I_D vs time) of the multiterminal OEET. Low f , I_D versus V_D characteristics are independent on the G_n -to-channel distance, while the high f pulsing response (I_D vs time) depends on the G_n -to-channel distance. In the latter regime of operation, the system exhibits spatiotemporal properties. b) Small channel. $|Z|$ versus f is independent of the spatial configuration of the multiterminal system. The electrical characteristics (I_D vs V_D , and pulsing response) are independent of the G_n -to-channel distance. For low f I - V measurements, step delay time for voltage sweep is equal to 2 s. The high f pulsing measurements parameters are the following: gate pulse voltage amplitude = 500 mV, time width = 100 ms, time between pulses = 5000 ms, $V_S = 0$ mV, $V_D = -100$ mV. Large channel device: channel dimensions ($W \times L = 500 \times 15\,000 \mu\text{m}^2$), gate dimensions: ($A_G = 2000 \times 2000 \mu\text{m}^2$). Small channel device: channel dimensions ($W \times L = 20 \times 20 \mu\text{m}^2$), gate dimensions ($A_G = 2000 \times 2000 \mu\text{m}^2$).

distance between G_n and channel) are converging in the low frequency regime, and the (low frequency) I - V characteristics are independent of the spatial device arrangement. In the high-frequency regime, however, the IS spectra are divergent and the high-frequency pulsing response obtains spatial properties. For a small channel (Figure 4b), the IS spectra merge into a single curve, and the corresponding low- (I - V) and high-frequency response (pulsing) is practically independent of the spatial configuration of the system. It is clear from Figure 4 that the system geometry and its probing conditions define the emergence of spatiotemporal dynamics. It should also be noted that the transconductance g_m of the large and small OEET is $g_{m(l)} = 0.13$ mS and $g_{m(s)} = 3.6$ mS, respectively, and thus $g_{m(l)}/g_{m(s)} = 0.036$. The small g_m obtained in the case of the large OEET is due to the OEET geometries. Indeed, g_m is proportional to the transistor form factor, W/L . The dimensions of the large OEET device are $W_1 = 500 \mu\text{m}$ and $L_1 = 15\,000 \mu\text{m}$, which result in a form factor, $W_1/L_1 = 0.033$ while the dimensions of the small OEET are $W_s = 20 \mu\text{m}$ and $L_s = 20 \mu\text{m}$, which result in a form factor, $W_s/L_s = 1$. The reduction of the form factor from 1 to 0.033 quantitatively supports the reduced g_m . The key OEET parameter affecting the spatiotemporal response are the OEET dimensions. More in detail, i) the polymer should extend from the first to the last columns of the gate matrix in order to locally convert ions to electronic charges that are then transported into the semiconducting electronic phase of the polymer. ii) The polymer area that, in turn, define the OEET capacitance $C_{\text{OEET}} = C_V \times W \times L \times t$, where C_V is the volumetric capacitance—an intrinsic property of the polymer—and t the polymer thickness.

To gain more insight on the key design parameters, the system is modeled by considering the various components

such as the G_n gate electrodes, the electrolyte, and the OEET channel. The system is described by using a modular circuit approach displayed in Figure S3, Supporting Information. A single column of gates is considered and a Randles circuit (C_G in parallel to a resistance R_G , with C_G and R_G the gate capacitance and resistance) extracted from IS, is used to model each gate. The vertical gate-to-gate and gate-to-channel coupling is described by the ionic resistance R_{YY} . Similarly, the horizontal gate-to-gate coupling is described by R_{XX} . R_{YY} and R_{XX} are experimentally accessed by varying the distance between the gates, the electrolyte concentration, and geometries. Finally, the OEET channel is modeled as a transistor including a Randles circuit extracted from IS measurements, namely a capacitance, C_{Ch} , in parallel to a resistance, R_{Ch} . The C_{Ch} and R_{Ch} elements are partitioned at the source (C_S and R_S) and drain (C_D and R_D) side of the channel. In the case of the long-channel system, the PEDOT:PSS channel is divided into five subchannels ($L_{\text{SC}} = L/5$) which are spatially coupled to the G_n gates and define a columnar, OEET_X. Figure S3, Supporting Information, also shows the circuit model of both the long- and short-channel systems.

The comparison of the fabricated system showed in Figure 1b with the circuit model, provides direct evidence of the role of the electrolyte and ionic–electronic interactions, which results in the various coupling elements. The spatiotemporal properties of the system depend on the balance between the gate capacitance, the distance between the various components (e.g., gate-to-gate and gate-to-channel), the electrolyte concentration, and the channel geometrical dimensions and capacitance. Focusing on the long-channel system, we used the model to investigate the impact of two key system parameters: the gate capacitance C_G and the vertical gate distance ΔY (here shown

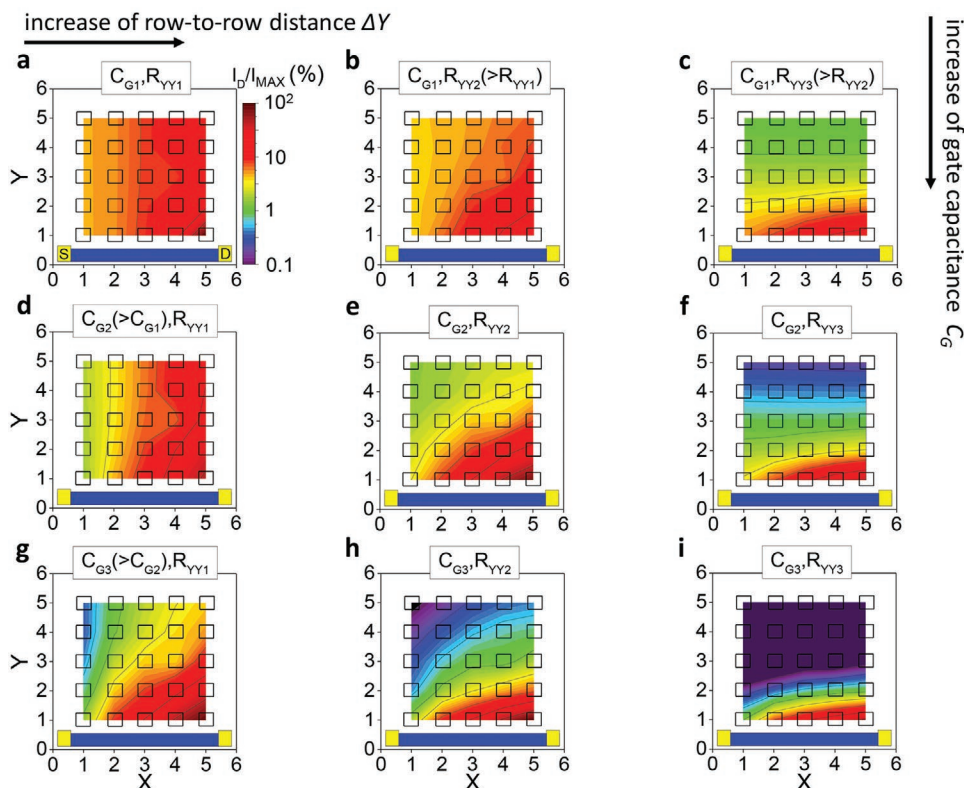


Figure 5. Impact of the system parameters on the spatiotemporal response. Spatial mapping of the percentage peak current normalized to the global maximum I_D/I_{MAX} (%). Logarithmic scale is used. The gate capacitance C_G , and distance between the gates along the vertical (Y) direction are varied (here shown as gate-to-gate resistance R_{YY}). By observing the subpanels across the horizontal direction, the vertical gate distance ΔY (or R_{YY}) is increasing, while moving across the subpanels in the vertical direction, C_G is increasing. a) $C_{G1} = 9.85 \times 10^{-6}$ F, $\Delta Y_1 = 175 + 700Y \mu\text{m}$ (or $R_{YY1} = 10.3$ Ohm), $Y = 0-4$. b) $C_{G1} = 9.85 \times 10^{-6}$ F, $\Delta Y_2 = 1750 + 7000Y \mu\text{m}$ (or $R_{YY2} = 103$ Ohm). c) $C_{G1} = 9.85 \times 10^{-6}$ F, $\Delta Y_3 = 17\ 500 + 70\ 000Y \mu\text{m}$ (or $R_{YY3} = 1030$ Ohm). d) $C_{G2} = 98.5 \times 10^{-6}$ F, $\Delta Y_1 = 175 + 700Y \mu\text{m}$. e) $C_{G2} = 98.5 \times 10^{-6}$ F, $\Delta Y_2 = 1750 + 7000Y \mu\text{m}$, that is, parameters of the experimental systems. f) $C_{G2} = 98.5 \times 10^{-6}$ F, $\Delta Y_3 = 17\ 500 + 70\ 000Y \mu\text{m}$. g) $C_{G3} = 985 \times 10^{-6}$ F, $\Delta Y_1 = 175 + 700Y \mu\text{m}$. h) $C_{G3} = 985 \times 10^{-6}$ F, $\Delta Y_2 = 1750 + 7000Y \mu\text{m}$. i) $C_{G3} = 985 \times 10^{-6}$ F, $\Delta Y_3 = 17\ 500 + 70\ 000Y \mu\text{m}$. All the other geometrical and physical parameters are the same of those obtained from the experimental long-channel system, $W = 500 \mu\text{m}$, $L = 15\ 000 \mu\text{m}$, $K_p = 14 \times 10^{-3} \text{ A V}^{-2}$, $V_T = 0.75 \text{ V}$.

as R_{YY}). In order to directly compare the various results, we calculated the percentage response of the output peak current, I_D/I_{MAX} (%), in respect to the global maximum peak, I_{MAX} , obtained by applying the input signal at a G_n gate of the grid. The spatial mappings of I_D/I_{MAX} (%), by varying C_G and R_{YY} , is shown in Figure 5. To highlight the impact of the parameters, both C_G and R_{YY} are increased/reduced by one order of magnitude with respect to the values obtained by modeling the experimental long-channel system while all the other system parameters are fixed (Table S1, Supporting Information).

In the limit of densely spaced gate rows and low gate capacitance, C_G , (upper left diagonal subpanel[s] of Figure 5, or Figure 5a,b,d) I_D/I_{MAX} (%) is independent on Y -direction. The system practically shows only very limited spatiotemporal response due to the ultralow response time across the Y -direction in respect to the probing conditions. In contrast, the spatiotemporal response across the X -direction is attributed to the polymeric channel. Ions transported through the electrolyte reach the channel and are converted into bulk electronic current. This is a spatial phenomenon that takes place along various positions of the channel length, depending on the horizontal position of the gate. The electronic charge carriers

that originate closer to the source electrode are transported for longer distances with respect to the ones originated closer to the drain, where the electronic current is measured. The spatiotemporal response is emerging when the row-to-row distance ΔY is increasing (across the horizontal subpanel direction). In the limit of large ΔY distances (Figure 5c,f,k) the spatiotemporal dependence is diminished for distant rows, from which the channel appears as a point device. The spatiotemporal response across Y -direction can also be recovered by increasing the gate capacitance C_G (across the vertical subpanel direction), and thus by increasing the response time across this direction. The analysis shows that optimal conditions are achieved in the case of Figure 5e (fabricated system) where 2D spatiotemporal response is displayed by all G_n gates.

The calculations of the Figure 5 show that the spatiotemporal response (viz. OECT current) reduces by increasing the gate-channel distance (parameter R_{YY}) and this can be tuned by changing the size of the most distanced electrodes. More in detail, for a given C_G , the spatiotemporal response increases by increasing the vertical distance but the current obtained from the most distanced gates vanishes and cannot be practically detected anymore (see e.g., Figure 5c,f,k). By increasing

C_G the spatiotemporal response can be enhanced but an optimum response depends on the gate distance. At small distances (Figure 5a,d,g) the maximum spatiotemporal response is achieved with the maximum C_G , while at larger distances (Figure 5b,e,h) larger capacitances could result in a limited response of the most distanced gates (Figure 5h) and the optimum is obtained when $C_G = C_{G2}$, $C_{G2} = 98.5 \times 10^{-6}$ F. Further increasing the gate-to-channel distance results in limited current response of about half of the gates and the increasing C_G is counter-productive (Figure 5c,f,k).

A deeper analysis on the impact of the channel length and the gate capacitance on the spatiotemporal response is shown in Figure S4, Supporting Information. The impact of the W/L ratio on the spatiotemporal response is also studied in Figure S4, Supporting Information. The spatiotemporal response depends on two key channel parameters, namely the channel length and the channel area. A long channel is essential to obtain a spatially distributed ion transduction along the channel, which result in a spatial time response. The channel area is directly related to the channel capacitance which affects the amount of ions flowing through the electrolyte upon the applied gate pulse. As a result, the channel length, L , and the channel area, $W \times L$, are important device parameters while the ratio, W/L , impact the magnitude of the drain current but has no impact on the spatiotemporal response of the device. Overall, optimal spatiotemporal response requires a balanced design between the electronic-to-ionic conversion at the gates, the ionic transport through the electrolyte, the ionic-to-electronic conversion along the channel, and the electronic transport through the channel. As shown from Figure S4, Supporting Information, the multiterminal device can be further scaled down. Apart from its applicability in the proposed system, it is noteworthy that the model can extend the proposed concept in a variety of materials/geometries and can be used as a universal tool for design and validation.

According to the aforementioned analysis, the large channel providing the optimized spatiotemporal response is used for the demonstration of ionic–electronic signal multiplexing. In **Figure 6**, the gates, G_n ($n = 1-25$), are randomly addressed by applying square voltage pulses (input signals) at each G_n sequentially. Details about the custom-made, accessing/measurement set-up are presented in the Supporting Information, and measurement conditions are described in Experimental Section. The amplitude of the output drain current I_D is also defined for every addressing event. The random accessing process is monitored and represented across the two directions of the 5×5 G_n grid in Figure 6a. The amplitude of I_D is represented by scanning across the rows of the G_n grid (Y -direction, for $Y = 1-5$ or row #). Despite the random G_n accessing process, Figure 6b shows that I_D amplitudes are accumulated in five distinct distributions that correspond to the rows of the 5×5 G_n grid. The response of accumulated I_D amplitudes of each row (X -direction or column #, for $Y = 1-5$ or row #) is shown in Figure 6c. The iontronic multiplexer is able to discriminate random inputs across the X -direction, with I_D amplitudes to be accumulated in distinct ranges that increase across X -direction. For distant rows (row #5), however, the ability for X -axis discrimination is suppressed, due to the fact that the channel appears as a point device. The theoretical distribution of I_D , as

predicted by the modular model, is also indicated in Figure 6b,c (x symbols) highlighting the effectiveness of the circuit model to simulate and predict the experimental behavior of the iontronic multiplexer.

3. Discussion

In this work, we demonstrated a bio-inspired iontronic multiplexer based on spatiotemporal dynamics of multiterminal OECTs. Inspired by biological systems, an electrolyte is the communication medium of the iontronic multiplexer. Electrolyte gating of the channel with a grid of gates allows for the formation of “virtual” wires in the electrolyte continuum that exhibit an Ohmic-like behavior. The configuration of the proposed iontronic multiplexer defines an all-to-one connectivity between the inputs and output, with inputs that are channelized through the spatiotemporal device dynamics and are readily differentiated at the output. The system exhibits a well-defined spatiotemporal response and predictable behavior as confirmed by the physical-based iontronic circuit model. Although the proposed model has been validated for a specific set of materials and electrolytes, it also has great predictive value and can be used universally in a greater family of materials consisting of mixed-conductors and electrolytes (e.g., organic or inorganic materials and solid or liquid electrolytes). Owing to the spatiotemporal response of the output current, the intrinsic properties of the system, namely the distance-dependent G_n -channel coupling, open possibilities for blind and local multiplexing of ionic–electronic signals. The term “blind” means that the output inherently depends on the spatial arrangement of the source of the electrical perturbation, without a-priori knowledge of the address of a gate, G_n . Multiplexing is also local, meaning that is readily incorporated in the spatiotemporal properties, and it does not result as a complex access circuitry, as for example in current passive or active matrices.

The blind and local iontronic multiplexing can be used for applications when simplicity and compactness is preferred against circuit complexity, as it decreases significantly the complexity in access and reading processes of spatially distributed signal sources (i.e., [bio]sensors or biological entities). Therefore, our approach finds relevant application in various emerging application fields including bioelectronics, wearables, e-skins, and neuromorphic sensors, where minimization of physical wiring and peripheral circuitry is essential for compact communication between the sensing and processing modalities.^[44,54–56] In addition, the proposed iontronic system can be extended for multiplexing of temporally sparse or even asynchronous, impulse-like input signals of fixed amplitude, such as in the case of spiking neural networks and time/frequency-domain coding of information.^[57–59] The reverse process of spatial reconstruction requires the detection of output current levels, which are directly related to the position of a signal source.

We also note that complementary information can be retrieved by gating multiple channels in perpendicular orientations with a grid of gate electrodes, thus enhancing fidelity and error-tolerance in input signal detection. Any limitations of the output current detection for long gate–channel distances can be mitigated by modifying the gate capacitance. Soft, solid-state

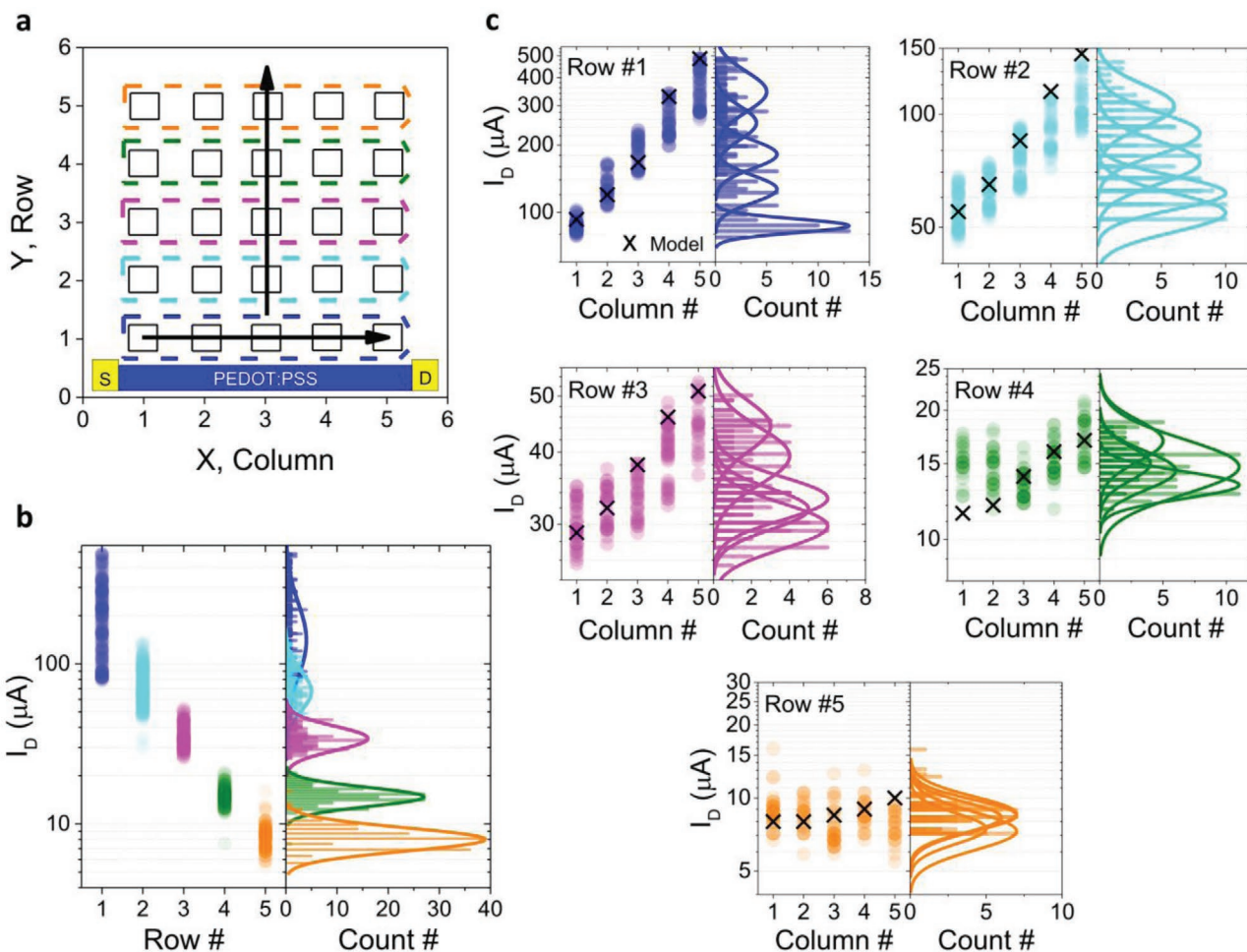


Figure 6. Local multiplexing of ionic–electronic signals. a) The gates, G_n ($n = 1–25$), of the iontronic multiplexer are randomly addressed by applying square voltage pulses (input signals) at each G_n sequentially (pulse amplitude: 500 mV, pulse width: 100 ms, in total ≈ 1000 access events), and the amplitude of the output current I_D is defined by measuring the drain current ($V_D = -100$ mV). I_D during the random G_n accessing is represented across X- and Y-direction. b) Distribution of I_D (amplitude of I_D and the corresponding Gaussian fit) by scanning events across the rows of the G_n grid (Y-direction, row #). c) Distribution of I_D (amplitude of I_D and the corresponding Gaussian fit) of each row (X-direction, column # for each row #). Position on the 5×5 G_n gate grid and I_D are color-coded accordingly. The theoretical distribution of I_D as predicted by the modular model is also indicated (x symbol). The system is able to discriminate random input events in the 2D space. NaCl electrolyte at concentration $c = 100$ mM is used.

electrolytes for gating OECTs, including polyelectrolytes and ionic gels are readily available,^[60–62] enabling potentially conformal multiplexing media. Electrolytes also exhibit volumetric conductivity, therefore even allow for 3D multiplexing when used as shared medium. Finally, the electrochemical nature of the shared medium of communication offers degrees of freedom that are inaccessible when multiplexing with conductive/metal tracks. As an example, the concept can be further extended beyond ionic to biochemical multiplexing, as the system’s various terminals can be selectively functionalized aiming for different sensing modalities in a host environment.

4. Experimental Section

Device Fabrication: The devices were fabricated using standard microfabrication techniques. Source, drain, and gate electrodes were patterned on 26 mm \times 76 mm microscope glass slides which were assiduously cleaned first in a soap (Micro-90) and then in a 1:1 (v/v)

solvent mixture (acetone/isopropanol) sonication bath. The gold (Au) electrodes were patterned via photolithography and the use of photoresist (S1813). Two layers of Parylene C were subsequently used to electrically insulate the device. Between these layers an anti-adhesive layer (Micro-90 soap solution, 1% v/v in deionized water) was deposited in order to facilitate a later peel-off step. Contrariwise, an adhesion promoter (silane A-174 [γ -methacryloxypropyltrimethoxysilane]), was employed between the substrate and the first Parylene C layer in order for the adhesion to be enhanced. A different photoresist (AZ 9260) was afterward spun on top of the two Parylene C layers and a second photolithography/development step defined window openings on the photoresist. Reactive ion etching with O_2/CF_4 plasma was used to remove Parylene C under those window openings and to create both the transistor channel and their corresponding gates. PEDOT:PSS was afterward spun creating a thin film of a conducting polymer that connected source and drain and coated the gate’s active area, resulting in a PEDOT:PSS film of thickness ≈ 500 nm. The subsequent peel-off step defined both the transistor’s channel and the gate electrodes. The external metal lines were protected under the insulating Parylene C layer. Finally, the devices were hard baked for an hour at 140 $^\circ$ C and placed in deionized water over night for the removal of the excess of

any low molecular weight molecules. Following the fabrication protocol described above, both large ($W \times L = 500 \mu\text{m} \times 15\,000 \mu\text{m}$) and small ($W \times L = 20 \mu\text{m} \times 20 \mu\text{m}$) multiterminal devices were fabricated. The gate grid was the same in both cases, with dimensions for each gate electrode ($2000 \mu\text{m} \times 2000 \mu\text{m}$) and center-to-center spacing, $8000 \mu\text{m}$. Each gate row was at a distance from the channel that equals to $1750 + 7000 \cdot Y$ (μm), with $Y = 2-5$, the number of gate row (detailed schematic of the dimensions is depicted in Figure S1, Supporting Information). PEDOT:PSS formulation: 38 mL of PEDOT:PSS aqueous dispersion (Clevios PH-1000), 2 mL of ethylene glycol (conductivity enhancement), 50 μL of 4-dodecylbenzenesulfonic acid (film formation), and 0.4 mL of 3-methacryloxypropyl-trimethoxysilane (surface adhesion promoter and polymer cross-linking agent).

Device Characterization: All measurements of the multiterminal OECT were performed with an aqueous NaCl electrolyte, at various concentrations ($c = 5-500 \text{ mM}$). Electrochemical IS measurements were realized with an impedance analyzer (PalmSens4). Typically, IS spectra were acquired in a frequency range = 50 mHz–100 kHz and with an amplitude of the AC signal = 25 mV. During the experiments, polydimethylsiloxane wells were used to confine the electrolyte. Source and drain electrodes were shorted and the PEDOT:PSS film was operated as the working electrode in a three electrode configuration set-up, where S and D electrodes were on the same potential and the channel was effectively operated as an electrode. A thin platinum (Pt) sheet was the reference electrode. Each of the 25 gold gate electrodes, covered with PEDOT:PSS, was the counter electrode. In the multiterminal OECT configuration, each device with 25 gates resulted in 25 impedance spectra in total. Low frequency $I-V$ characteristics of the multiterminal OECTs, were performed with a semiconductor analyzer (Keithley 4200A-SCS) and source measure units. High-frequency pulsed measurements were performed with a custom-built set-up (refer to Supporting Information): a custom-made, electronic board with 25 pulsing units was used for applying pulses at the gate electrodes (inputs: I), while resulting output current (output: O) was measured, a semiconductor analyser (Keithley 4200A-SCS), at the drain electrode (D) with the source electrode (S) being grounded. The electronic board was synchronized with the semiconductor analyser with time triggering. Blind multiplexing measurements were performed with this configuration and a software to control the electronic board that was randomly and sequentially assigning gate addresses and applying random input pulses at each gate electrode. As a result of this random gate addressing, the output current was measured with the semiconductor analyser (Keithley 4200A-SCS).

Analysis: Data plotting, as well as the corresponding analysis (peak analysis of the output current, equivalent circuit modeling of the IS spectra) was performed in OriginPro 2016. Peak analysis was performed with a threshold of 2–5% of the maximum for output current peak detection, after subtracting the background current (2–5% threshold was found to be adequate for reliable detection of output peaks from background noise). Circuit modeling of the IS spectra was performed with a series RC circuit. Additional equivalent circuit modeling was performed with the impedance analyser software (PSTrace). Modeling of the $I-V$ and pulsed $I-t$ characteristics of the multiterminal OECT was performed with MATLAB. Circuit simulations were performed by including the custom models in Cadence Virtuoso software.

Supporting Information

Supporting Information is available from the Wiley Online Library or from the author.

Acknowledgements

D.A.K. and M.H.A. contributed equally to this work. The authors acknowledge George Malliaras for fruitful discussions on the device physics of OECTs, Armantas Melianas for discussions on spatiotemporal

device response, and Javad Taghinasab for his assistance in designing the custom-made electronic board. The authors also wish to thank Hans-Juergen Guttman, Christian Bauer, Frank Keller and Michelle Beuchel and Katharina Lieberth from MPIP for their technical assistance. K.A. and M.H.A. acknowledge the financial support of the Alexander von Humboldt Foundation (Germany) through the Sofja Kovalevskaja Award, and the technical support from the Max-Planck Institute for Polymer Research.

Open access funding enabled and organized by Projekt DEAL.

Conflict of Interest

The authors declare no conflict of interest.

Data Availability Statement

Data available on request by the authors.

Keywords

bioelectronics, electrolytes, mixed conductors, neuromorphic electronics, organic electrochemical transistors, spatiotemporal response

Received: December 22, 2020

Revised: February 28, 2021

Published online: March 24, 2021

- [1] M. Mehrli, S. Bagherifard, M. Akbari, A. Thakur, B. Mirani, M. Mehrli, M. Hasany, G. Orive, P. Das, J. Erneus, T. L. Andresen, A. Dolatshahi-Pirouz, *Adv. Sci.* **2018**, *5*, 1700931.
- [2] T. Someya, Z. Bao, G. G. Malliaras, *Nature* **2016**, *540*, 379.
- [3] S. Vassanelli, M. Mahmud, *Front. Neurosci.* **2016**, *10*, 438.
- [4] C. Lubrano, G. M. Matrone, C. Forro, Z. Jahed, A. Offenhaeusser, A. Salleo, B. Cui, F. Santoro, *MRS Commun.* **2020**, *10*, 398.
- [5] E. R. Kandel, J. H. Schwartz, T. M. Jessell, *Principles of Neural Science*, McGraw-Hill, New York **2000**.
- [6] V. E. Abraira, D. D. Ginty, *Neuron* **2013**, *79*, 618.
- [7] N. Spruston, W. L. Kath, *Nat. Neurosci.* **2004**, *7*, 567.
- [8] T. Branco, B. A. Clark, M. Häusser, *Science* **2010**, *329*, 1671.
- [9] G. Buzsáki, B. O. Watson, *Dialogues Clin. Neurosci.* **2012**, *14*, 345.
- [10] N. Gupta, S. S. Singh, M. Stopfer, *Nat. Commun.* **2016**, *7*, 13808.
- [11] J. Fell, N. Axmacher, *Nat. Rev. Neurosci.* **2011**, *12*, 105.
- [12] J. A. Roberts, L. L. Gollo, R. G. Abey Suriya, G. Roberts, P. B. Mitchell, M. W. Woolrich, M. Breakspear, *Nat. Commun.* **2019**, *10*, 1056.
- [13] C. A. Anastassiou, R. Perin, H. Markram, C. Koch, *Nat. Neurosci.* **2011**, *14*, 217.
- [14] *Handbook of Visual Display Technology* (Eds: J. Chen, W. Cranton, M. Fihn), Springer, Berlin **2012**.
- [15] H. E. A. Huitema, G. H. Gelinck, J. B. P. H. van der Putten, K. E. Kuijk, C. M. Hart, E. Cantatore, P. T. Herwig, A. J. J. M. van Breemen, D. M. de Leeuw, *Nature* **2001**, *414*, 599.
- [16] G. H. Gelinck, H. E. A. Huitema, E. van Veenendaal, E. Cantatore, L. Schrijnemakers, J. B. P. H. van der Putten, T. C. T. Geuns, M. Beenhakkers, J. B. Giesbers, B.-H. Huisman, E. J. Meijer, E. M. Benito, F. J. Touwslager, A. W. Marsman, B. J. E. van Rens, D. M. de Leeuw, *Nat. Mater.* **2004**, *3*, 106.
- [17] M. Prezioso, F. Merrikh-Bayat, B. D. Hoskins, G. C. Adam, K. K. Likharev, D. B. Strukov, *Nature* **2015**, *521*, 61.
- [18] S. Ambrogio, P. Narayanan, H. Tsai, R. M. Shelby, I. Boybat, C. di Nolfo, S. Sidler, M. Giordano, M. Bodini, N. C. P. Farinha, B. Killeen, C. Cheng, Y. Jaoudi, G. W. Burr, *Nature* **2018**, *558*, 60.

- [19] E. J. Fuller, S. T. Keene, A. Melianas, Z. Wang, S. Agarwal, Y. Li, Y. Tuchman, C. D. James, M. J. Marinella, J. J. Yang, A. Salleo, A. A. Talin, *Science* **2019**, *364*, 570.
- [20] M. Hu, J. P. Strachan, Z. Li, E. M. Grafals, N. Davila, C. Graves, S. Lam, N. Ge, J. J. Yang, R. S. Williams, in *2016 53rd ACM/EDAC/IEEE Design Automation Conf. (DAC)*, IEEE, Piscataway, NJ **2016**, 1.
- [21] Y. van de Burgt, A. Melianas, S. T. Keene, G. Malliaras, A. Salleo, *Nat. Electron.* **2018**, *1*, 386.
- [22] Q. Xia, J. J. Yang, *Nat. Mater.* **2019**, *18*, 309.
- [23] J. Viventi, D.-H. Kim, L. Vigeland, E. S. Frechette, J. A. Blanco, Y.-S. Kim, A. E. Avrin, V. R. Tiruvadi, S.-W. Hwang, A. C. Vanleer, D. F. Wulsin, K. Davis, C. E. Gelber, L. Palmer, J. Van der Spiegel, J. Wu, J. Xiao, Y. Huang, D. Contreras, J. A. Rogers, B. Litt, *Nat. Neurosci.* **2011**, *14*, 1599.
- [24] T. Someya, T. Sekitani, S. Iba, Y. Kato, H. Kawaguchi, T. Sakurai, *Proc. Natl. Acad. Sci. USA* **2004**, *101*, 9966.
- [25] W. W. Lee, Y. J. Tan, H. Yao, S. Li, H. H. See, M. Hon, K. A. Ng, B. Xiong, J. S. Ho, B. C. K. Tee, *Sci. Rob.* **2019**, *4*, eaax2198.
- [26] T. Sekitani, T. Yokota, U. Zschieschang, H. Klauk, S. Bauer, K. Takeuchi, M. Takamiya, T. Sakurai, T. Someya, *Science* **2009**, *326*, 1516.
- [27] J. J. Yanga, M.-X. Zhang, M. D. Pickett, F. Miao, J. P. Strachan, W.-D. Li, W. Yi, D. A. A. Ohlberg, B. J. Choi, W. Wu, J. H. Nickel, G. Medeiros-Ribeiro, R. S. Williams, *Appl. Phys. Lett.* **2012**, *100*, 113501.
- [28] K. Asadi, M. Li, N. Stingelin, P. W. M. Blom, D. M. de Leeuw, *Appl. Phys. Lett.* **2010**, *97*, 193308.
- [29] R. Garcia-Cortadella, N. Schäfer, J. Cisneros-Fernandez, L. Ré, A. Illa, G. Schwesig, A. Moya, S. Santiago, G. Guirado, R. Villa, A. Sirota, F. Serra-Graells, J. A. Garrido, A. Guimerà-Brunet, *Nano Lett.* **2020**, *20*, 3528.
- [30] W. E. Vinje, J. L. Gallant, *Science* **2000**, *287*, 1273.
- [31] T. Hromádka, M. R. DeWeese, A. M. Zador, *PLoS Biol.* **2008**, *6*, e16.
- [32] S. Crochet, J. F. A. Poulet, Y. Kremer, C. C. H. Petersen, *Neuron* **2011**, *69*, 1160.
- [33] I. Ito, R. C.-Y. Ong, B. Raman, M. Stopfer, *Nat. Neurosci.* **2008**, *11*, 1177.
- [34] M. A. Sivilotti, *Ph.D. Wiring Considerations in Analog VLSI Systems, with Application to Field-Programmable Networks*, California Institute of Technology **1991**.
- [35] M. Mahowald, *Ph.D. VLSI Analogs of Neuronal Visual Processing: A Synthesis of Form and Function*, California Institute of Technology **1992**.
- [36] K. A. Boahen, *IEEE Trans. Circuits Syst.* **2000**, *47*, 416.
- [37] S.-C. Liu, T. Delbruck, G. Indiveri, A. Whatley, R. Douglas, *Event-Based Neuromorphic Systems*, Wiley, West Sussex, UK **2015**.
- [38] L. Herlogsson, X. Crispin, N. D. Robinson, M. Sandberg, O.-J. Hagel, G. Gustafsson, M. Berggren, *Adv. Mater.* **2007**, *19*, 97.
- [39] P. Gkoupidenis, D. A. Koutsouras, T. Lonjaret, J. A. Fairfield, G. G. Malliaras, *Sci. Rep.* **2016**, *6*, 27007.
- [40] P. Gkoupidenis, D. A. Koutsouras, G. G. Malliaras, *Nat. Commun.* **2017**, *8*, 15448.
- [41] H. Ling, D. A. Koutsouras, S. Kazemzadeh, Y. van de Burgt, F. Yan, P. Gkoupidenis, *Appl. Phys. Rev.* **2020**, *7*, 011307.
- [42] A. Stoddart, *Nat. Rev. Mater.* **2018**, *3*, 18014.
- [43] J. Rivnay, S. Inal, A. Salleo, R. M. Owens, M. Berggren, G. G. Malliaras, *Nat. Rev. Mater.* **2018**, *3*, 17086.
- [44] E. R. W. van Doremaele, P. Gkoupidenis, Y. van de Burgt, *J. Mater. Chem. C* **2019**, *7*, 12754.
- [45] Y. van de Burgt, P. Gkoupidenis, *MRS Bull.* **2020**, *45*, 631.
- [46] Y. Tuchman, T. N. Mangoma, P. Gkoupidenis, Y. van de Burgt, R. A. John, N. Mathews, S. E. Shaheen, R. Daly, G. G. Malliaras, A. Salleo, *MRS Bull.* **2020**, *45*, 619.
- [47] B. D. Paulsen, K. Tybrandt, E. Stavrinidou, J. Rivnay, *Nat. Mater.* **2020**, *19*, 13.
- [48] J. Rivnay, P. Leleux, M. Ferro, M. Sessolo, A. Williamson, D. A. Koutsouras, D. Khodagholy, M. Ramuz, X. Strakosas, R. M. Owens, C. Benar, J.-M. Badiet, C. Bernard, G. G. Malliaras, *Sci. Adv.* **2015**, *1*, e1400251.
- [49] D. A. Bernards, G. G. Malliaras, *Adv. Funct. Mater.* **2007**, *17*, 3538.
- [50] D. A. Koutsouras, T. Prodromakis, G. G. Malliaras, P. W. M. Blom, P. Gkoupidenis, *Adv. Intell. Syst.* **2019**, *1*, 1900013.
- [51] D. A. Koutsouras, P. Gkoupidenis, C. Stolz, V. Subramanian, G. G. Malliaras, D. C. Martin, *ChemElectroChem* **2017**, *4*, 2321.
- [52] D. A. Koutsouras, L. V. Lingstedt, K. Lieberth, J. Reinholz, V. Mailänder, P. W. M. Blom, P. Gkoupidenis, *Adv. Healthcare Mater.* **2019**, *8*, 1901215.
- [53] J. Maier, *Prog. Solid State Chem.* **1995**, *23*, 171.
- [54] P. Li, H. P. A. Ali, W. Cheng, J. Yang, B. C. K. Tee, *Adv. Mater. Technol.* **2020**, *5*, 1900856.
- [55] P. Jastrzebska-Perfect, S. Chowdhury, G. D. Spyropoulos, Z. Zhao, C. Cea, J. N. Gelinias, D. Khodagholy, *Adv. Funct. Mater.* **2020**, *30*, 1909165.
- [56] Y. Kim, A. Chortos, W. Xu, Y. Liu, J. Y. Oh, D. Son, J. Kang, A. M. Foudeh, C. Zhu, Y. Lee, S. Niu, J. Liu, R. Pfattner, Z. Bao, T.-W. Lee, *Science* **2018**, *360*, 998.
- [57] K. Roy, A. Jaiswal, P. Panda, *Nature* **2019**, *575*, 607.
- [58] H. H. See, B. Lim, S. Li, H. Yao, W. Cheng, H. Soh, B. C. K. Tee, <https://arxiv.org/abs/2005.04319>, **2020**.
- [59] C. Mead, *Nat. Electron.* **2020**, *3*, 434.
- [60] K. H. Lee, M. S. Kang, S. Zhang, Y. Gu, T. P. Lodge, C. D. Frisbie, *Adv. Mater.* **2012**, *24*, 4457.
- [61] A. Melianas, T. J. Quill, G. LeCroy, Y. Tuchman, H. v. Loo, S. T. Keene, A. Giovannitti, H. R. Lee, I. P. Maria, I. McCulloch, A. Salleo, *Sci. Adv.* **2020**, *6*, eabb2958.
- [62] G. D. Spyropoulos, J. N. Gelinias, D. Khodagholy, *Sci. Adv.* **2019**, *5*, eaau7378.